

# A wide-field study of globular clusters in the nearest giant elliptical: Subaru/Suprime-Cam observations of Maffei 1\*

Samuel Hinton<sup>1,2</sup>, Ricardo Salinas<sup>3</sup> Aaron J. Romanowsky<sup>4,5</sup>, and maybe some others

<sup>1</sup>School of Mathematics and Physics, University of Queensland, QLD 4072, Australia

<sup>2</sup>Australian Astronomical Observatory, North Ryde, NSW 2113, Australia

<sup>3</sup>Gemini Observatory

<sup>4</sup>Department of Physics & Astronomy, San José State University, San Jose, CA 95192, USA

<sup>5</sup>University of California Observatories, 1156 High Street, Santa Cruz, CA 95064, USA

Accepted ... Received ...; in original form ...

## ABSTRACT

Lorem ipsum dolor sit amet, consectetur adipiscing elit. Sed condimentum ipsum faucibus sem elementum, eu consectetur risus consectetur. Praesent quis aliquam risus. Vivamus interdum et eros gravida rhoncus. Proin accumsan finibus pellentesque. Praesent et erat eu velit maximus condimentum. Integer ornare vestibulum dolor nec pretium. Suspendisse suscipit, metus sed consectetur pretium, ligula nunc mollis quam, id dapibus est tortor et massa. Mae- cenas maximus elit orci, sit amet tincidunt libero ultrices a. Nullam sit amet condimentum libero. Duis ullamcorper lorem in nisi gravida tincidunt. Aliquam erat volutpat. Sed vitae sem a elit mattis porttitor.

**Key words:** Galaxies: individual: Maffei 1 – Galaxies: star clusters

## 1 INTRODUCTION

### Add some general remarks on globular cluster systems.

Maffei 1 is a giant elliptical galaxy (Maffei 1968; Spinrad et al. 1971) located at only  $0.5^\circ$  North of the Galactic plane. This position implies large obscuration by dust from the Galactic disc which has hampered the measurement of even the most basic parameters of the galaxy.

### Give main results from the literature

Its particular relative position has also conspired against the study of its globular clusters (GCs). Studies of its globular cluster system (GCS) have produced only a handful of GC candidates (Davidge 2002; Buta & McCall 2003; Davidge & van den Bergh 2005), whereas for its luminosity ( $M_V \sim -20.80$ , Fingerhut et al. 2007), the size of its GCS should be comparable to the one of Cen A, hosting  $\sim 1300$  GCs (Harris 2010).

In this paper we present the first wide-field study of the Maffei 1 GCS system using Subaru/SuprimeCam imaging. In Sect. 2 we present the imaging data used, as well as its reduction and photometry. In Sect. 3 we present the GCs selection, together with the derived properties of the GCS. Sect. 4 puts our results on a wider context, while Sect. 5 summarizes the work and give conclusions.

## 2 SUBARU/SUPRIME-CAM OBSERVATIONS AND DATA REDUCTION

Maffei 1 images were obtained using Suprime-Cam (Miyazaki et al. 2002) located on the Subaru telescope, Mauna Kea, Hawaii. Suprime-Cam comprises 10 CCD detectors separated by  $\sim 15''$  covering a field-of-view of  $34' \times 27'$  with a pixel scale of  $0.2''$ . SDSS  $r'$ ,  $i'$  and  $z'$ -band images were obtained during the night of January 5th, 2011. Several short exposures were taken with a  $\sim 1'$  dither pattern, totalling 385, 280, and 280 seconds in the  $r'$ ,  $i'$  and  $z'$ -bands, respectively.

Suprime-Cam images reduction was conducted within the SD-FRED2 pipeline (Ouchi et al. 2004). Reduction steps include bias subtraction, flat-fielding, correction for atmospheric distortions, point spread function (psf) equalization (i.e. the normalization of the psf to a single shape across the detectors and exposures), sky subtraction, image alignment and finally, the combination of all exposures and detectors into single images. Final averaged images have a field-of-view of  $\sim 37' \times 31'$  and a seeing quality of  $0.72''$ ,  $0.68''$  and  $0.63''$ , for  $r'$ ,  $i'$  and  $z'$ , respectively. The field of view in  $z'$  is shown in Figure 1, and a detailed colour image of the galactic core is presented in Figure 2.

For the  $z'$  image set, which is used as the basis for the GC candidates identification given its higher image quality (see Sect. 3.1), a parallel alternative reduction process was adopted. The  $z'$  dataset not only provides the reddest band to pierce through the Galactic plane, but also contains the best seeing images. Even though the same SD-FRED2 pipeline was mostly used, a couple of the aforementioned reduction steps were skipped in order to maintain image manipulations that could alter the image quality to a minimum.

\* Based on data collected at Subaru Telescope, which is operated by the National Astronomical Observatory of Japan.

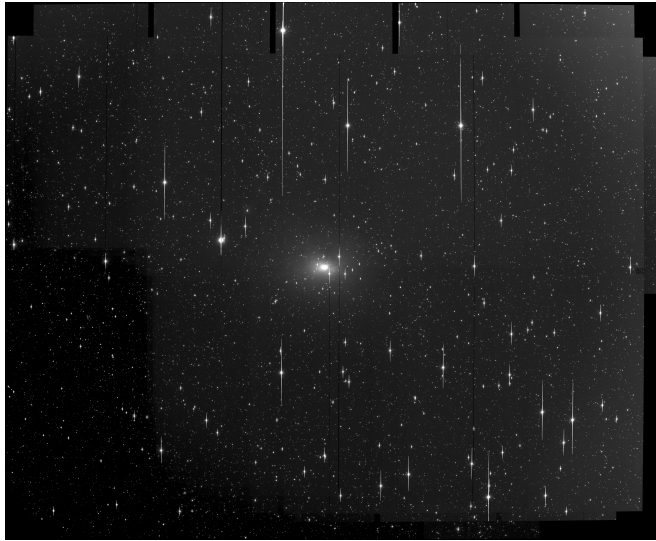


**Figure 1.** The Maffei 1 field as seen by Subaru-SuprimeCam in  $z'$ . Image size is approximately  $37' \times 31'$ . North is up and East is to the left.

Firstly, given the slight degradation of the psf towards the outer detectors, psf equalization across the chips would imply a loss of information on the best chips. For this reason the detectors were reduced independently and not combined into a single image as a final step. As a second difference, we did not apply any correction for atmospheric distortions, since it resulted in an increase of about 10% of the measured stellar full width at half maximum (fwhm) due to charge shifting to neighbor pixels. Finally, images with psf sizes significantly larger than the mean were excluded from the final image combination. This resulted in the rejection of zero to two exposures per chip.

Coordinate transformations and image combination for the individual detectors were carried out with DAOMASTER/MONTAGE2 (Stetson 1993, 1994), which give more flexibility than SDFRED2 for images with a small overlapping area. Measured fwhm on the combined  $z'$  images varies between  $0.52''$  to  $0.58''$  from detector to detector, which are noticeably better than the  $0.62''$  measured on the combined full frame image given by SDFRED2.

As a last step prior to initial photometry, images presenting large background variations (containing Maffei 1 light or Galactic cirrus), were median filtered with an annulus kernel, with outer radius size of 150 pixel and an inner radius of 105 pixels; a large size that preserves point-like sources unaltered. Photometry and astrometry were performed on the images fully processed with the SDFRED2 pipeline.

## 2.1 Stellar photometry

Manual aperture and psf-fitting photometry were carried out on a chosen example tile using the stand-alone DAOPHOT2 photometric suite (Stetson 1987). The psf was modelled selecting  $\sim 120$ – $140$  bright and isolated stars on each detector. A quadratically varying Moffat function was found to provide the best description of the psf behaviour within the detectors.

Photometry for all the sources was also obtained using SExtractor (Bertin & Arnouts 1996), which additionally provides measurements of the size, orientation and ellipticity of the sources.

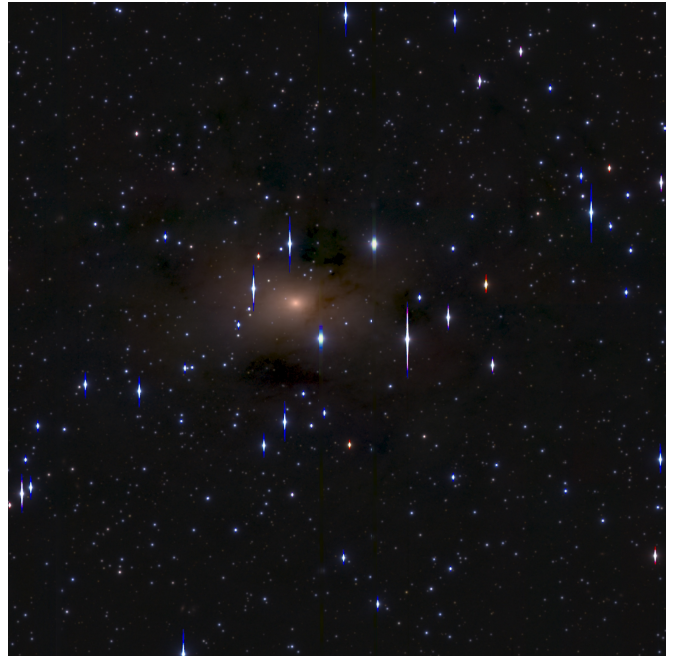


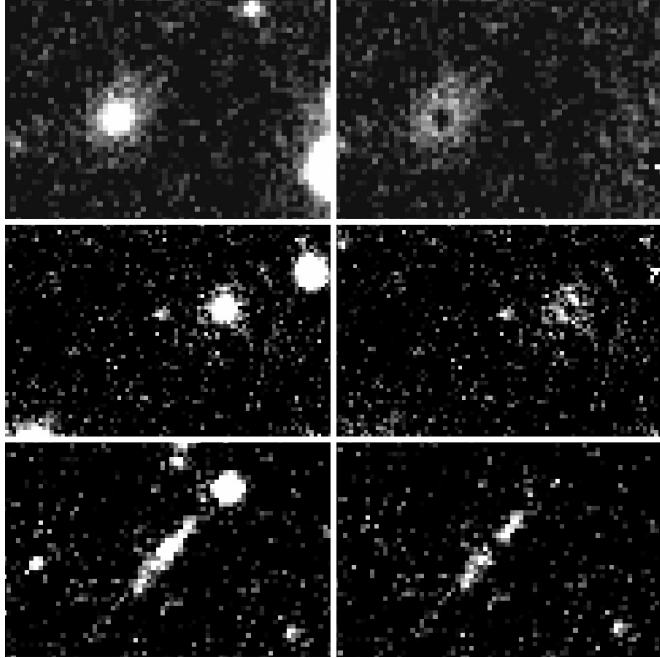
**Figure 2.** The core of Maffei 1 shown in  $z'$ ,  $i'$  and  $r'$ , generated by STIFF (Bertin 2012). The image size is approximately  $6.5' \times 6.5'$ . North is up and East is to the left.

## 3 RESULTS

### 3.1 Selecting globular clusters candidates

The basic selection criterion for GCs in Maffei 1 rests on the non-stellar shape of their light profiles. This shape, usually smeared out for distant systems or in images with low spatial resolution, should be noticeable for the largest GCs in Maffei 1 given the galaxy's distance and the quality of the imaging. A similar approach has been applied successfully on ground-based imaging of GCs in the slightly more distant elliptical galaxy Centaurus A (Rejkuba 2001; Gómez et al. 2006; Gómez & Woodley 2007). As manual inspection of all sources was infeasible due to the number of sources, a machine learning approach was adopted in order to differentiate between stellar sources and extended sources. Initially, the neural network classifier contained inside SExtractor was utilised, but a posterior analysis has shown that clearly resolved sources have been assigned a CLASS\_STAR parameter value as high as 0.98, which on a blind approach would have been classified as stars. Thus the algorithm was found to be insufficient, and a new algorithm was developed. Training of the machine learning algorithms was performed by combining artificially generated data and manual classification on a single tile.

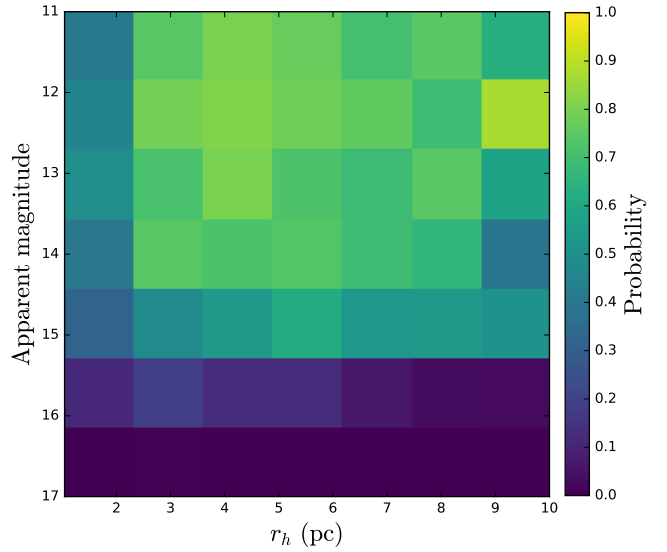
Manual classification was performed by visual analysis of the star-subtracted  $z'$ -image of the chosen CCD tile produced by the psf-fitting algorithm in ALLSTAR. The image was visually inspected to look for residuals that revealed the presence of extended sources. The light profile of GCs (but also galaxies) would be over-subtracted in the central parts and under-subtracted in the wings, leaving an easily recognizable “ring-shaped” residual (see Fig. 3). A visual inspection of the residuals in a tile is a painstaking process, but provides benefit over only artificial data that does not model the full distribution of extended sources accurately. Our selected approach revealed the presence of 77 extended sources in the Clarisse tile.



**Figure 3.** Three examples of the psf-subtraction technique applied on the final  $z$  images to reveal extended sources. The left panels show the original image, while the right panels are the psf-subtracted images. Top panels: A round object revealing a highly confident classification. Middle panels: A similar classification with a lower confidence due to the image noise. Bottom panels: An elongated extended object, in this case a galaxy viewed from the side, where the high ellipticity of the source allows differentiation between globular cluster and galaxy.

Artificial stars and extended sources were added to the Clarisse tile by the use of the `mksynth` task in BAOLAB (Larsen 1999). The psf input into the `mksynth` function was determined using by automatically selecting a number of candidate psf stars (based on flux criterion, star classification and source isolation), and generating a subsampled psf using the `digiphot` package in IRAF CITE. For generation of artificial extended objects, the `mkcmppsf` task was also used to generate a composite psf with a King model (King 1962) with concentration index of 30. The fwhm of the model was randomised to allow variation in the size of the artificial globular clusters. Both stars and extendeds were generated with uniform randomised magnitudes. The input data set was then created by using SExtractor to detect source properties of both the artificial sources and manually classified sources. In total, over 17 000 artificial globular cluster candidates and 170 000 artificial stars were introduced over a series of 300 artificial images to create a large set of data. The weighting of the manually detected stars and extended objects from the original tile was increased by a factor of a hundred to reflect their realism over artificial sources.

The input data was split into training, testing and validation sets, using ratios 0.4, 0.35 and 0.25 respectively, where multiple machine learning algorithms were trained on the training data, and the algorithm with the highest Matthews correlation coefficient (Matthews 1975) when evaluated on the validation set was selected as the final algorithm. The Matthews correlation coefficient was chosen to be maximised over other coefficients such as classifier accuracy, due to its fairness in dealing with unbalanced classes (Baldi et al. 2000; Jurman et al. 2012), which we expect to find with the number of point sources far exceeding the number of extended sources. Expected performance of the algorithm was determined

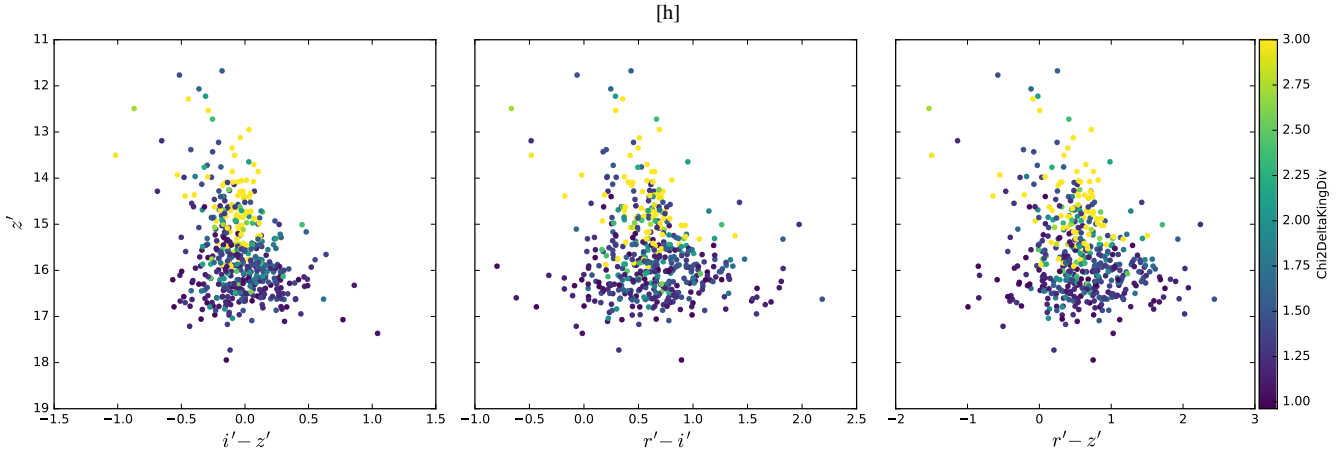
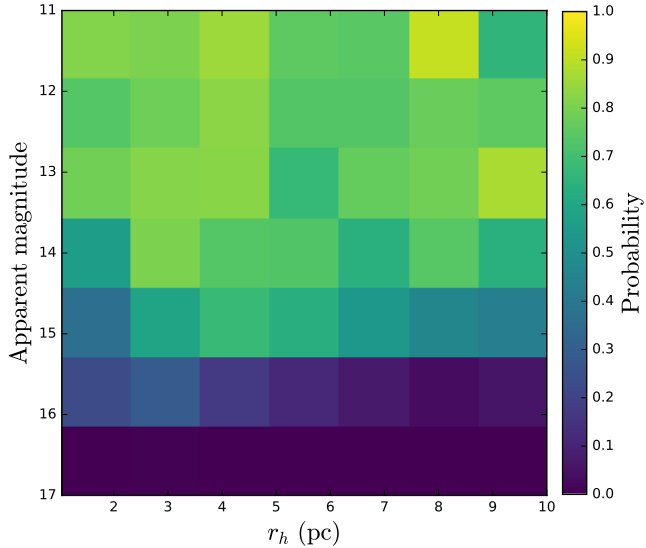


**Figure 5.** The probability  $P(r_h, \mu)$  of correctly classifying an extended object using the initial classifier supplied with data from SExtractor. Classification accuracy decreases as  $r_h$  decreases, as the source becomes more pointlike. Similarly, we notice that objects dimmer than a magnitude of **PUT THIS IN WHEN YOU KNOW THE ACTUAL MAGNITUDES** are not classified correctly, as they are not detected by SExtractor. The maximum detection rate found corresponds to a 90% chance of detection.

by fitting to the test data set, and the probability of correctly classifying an extended object as a function of half light radius and magnitude is shown in Figure 5.

The extended candidates for each tile given by the initial machine learning algorithm were then processed through the task `iShape`, a procedure in the BAOLAB software package, to gather more information on the candidates. This step is done separately as computational constraints hinder the ability to run `iShape` on all detected sources, and so an initial candidate round must be selected. Information on  $\chi^2$  of the King fit,  $\chi^2$  of the delta model fit, and the fwhm of the King profile are added to the original data set. The manually selected candidates and artificially generated sources were also processed by `iShape`, and the improved dataset was used to train a second classifier in a similar fashion to the first, which was designed to remove many of the false positives from the initial classifier and improve accuracy on only partially resolved globular cluster candidates. The probability of detecting a source as a globular cluster correctly, as a function of half light radius  $r_h$  and magnitude for the new classifier is shown in Figure 6. It important to note that the success rates shown in Figure 6 cannot be directly applied to the real data and thus only provide estimates. The matching accuracy on other tiles is expected to be lower due to artificial modelling not reflecting all the variations and subtleties of real global clusters and the lack of modelling other sources, such as compact dwarfs, stanard galaxies and other astronomical phenomenon outside stars and globular clusters.

Each candidate underwent aperture photometry on the fully reduced mosaics mentioned in Section 2, where colour magnitude corrections were performed by interpolating the dust maps from Schlegel et al. (1998) and applying the band extinction to redding ratios from Schlafly & Finkbeiner (2011). Magnitude calibration was performed by using the Landolt set of standard stars (Landolt 1992), that had been transformed via the equations given in Fukugita et al. (1996) into the SDSS system. **PUT MAGNITUDE**

**Figure 4.** Colours

**Figure 6.** The probability  $P(r_h, \mu)$  of correctly classifying an extended object using the secondary classifier, that is supplied with both data from SExtractor and data from ISHAPE fitting to a King profile. The fitting information allows increased discrimination between point sources and extended objects at lower values of  $r_h$ . The maximum chance of detection mirrors that found in Figure 5 at 90%.

#### BASELINE IN WHEN YOU DO IT. IT GOES BEFORE THE DUST CORRECTION MAYBE, ASK RICARDO

Further pruning of the globular cluster candidates was performed removing unphysical outliers in the analysis, such as removing objects with a detected fwhm of over a ten arcseconds. In addition, ellipticity cutoffs, colour profile cuts and magnitude cuts were introduced to remove galaxies in the globular cluster candidate list.

The extended sources were separated into 3 classes based on the visual appearance of their residuals in combination with their structural parameters measured with SExtractor: circular residuals with  $\text{fwhm} < XX$  (class A), symmetric but elongated residuals where the source has  $\epsilon < 0.3$  (class B), and finally, elongated residuals with  $\epsilon > 0.3$  together with sources with very extended ( $\text{fwhm} > 6$  pixels) or asymmetric residuals (class C). In the few

cases where the source was not detected by SExtractor (usually because of the proximity of a bright star or the patchy Maffei 1 center), the classification was made only based on their visual appearance. The ellipticity limit of 0.3 was chosen since it contains all the ellipticities found for GCs in Local Group galaxies (e.g. van den Bergh 2008). These classes correlate with the likelihood of the sources being genuine Maffei 1 GCs based on their structure, with the round class-A objects having a higher probability of being genuine Maffei 1 GCs, and the elongated or large class-C sources, being most probably background galaxies.

### 3.2 Globular clusters color-magnitude diagram

### 3.3 Globular cluster sizes

## 4 DISCUSSION

## 5 SUMMARY AND CONCLUSIONS

### ACKNOWLEDGMENTS

AJR was supported by National Science Foundation grants AST-0808099 and AST-0909237.

### REFERENCES

- Baldi P., Brunak S., Chauvin Y., Andersen C. A. F., Nielsen H., 2000, Bioinformatics, 16, 412
- Bertin E., 2012, in Ballester P., Egret D., Lorente N. P. F., eds, Astronomical Data Analysis Software and Systems XXI Vol. 461 of Astronomical Society of the Pacific Conference Series, Displaying Digital Deep Sky Images. p. 263
- Bertin E., Arnouts S., 1996, A&AS, 117, 393
- Buta R., McCall M. L., 2003, AJ, 125, 1150
- Davidge T. J., 2002, AJ, 124, 2012
- Davidge T. J., van den Bergh S., 2005, PASP, 117, 589
- Fingerhut R. L., Lee H., McCall M. L., Richer M. G., 2007, ApJ, 655, 814
- Fukugita M., Ichikawa T., Gunn J. E., Doi M., Shimasaku K., Schneider D. P., 1996, AJ, 111, 1748
- Gómez M., Geisler D., Harris W. E., Richtler T., Harris G. L. H., Woodley K. A., 2006, A&A, 447, 877
- Gómez M., Woodley K. A., 2007, ApJ, 670, L105

- Harris G. L. H., 2010, PASA, 27, 475
- Jurman G., Riccadonna S., Furlanello C., 2012, PLoS ONE, 7, e41882
- King I., 1962, AJ, 67, 471
- Landolt A. U., 1992, AJ, 104, 340
- Larsen S. S., 1999, A&AS, 139, 393
- Maffei P., 1968, PASP, 80, 618
- Matthews B. W., 1975, Biochimica et Biophysica Acta (BBA)-Protein Structure, 405, 442
- Miyazaki S., Komiya Y., Sekiguchi M., Okamura S., Doi M., Furusawa H., Hamabe M., Imi K., Kimura M., Nakata F., Okada N., Ouchi M., Shimasaku K., Yagi M., Yasuda N., 2002, PASJ, 54, 833
- Ouchi M., Shimasaku K., Okamura S., Furusawa H., Kashikawa N., Ota K., Doi M., Hamabe M., Kimura M., Komiya Y., Miyazaki M., Miyazaki S., Nakata F., Sekiguchi M., Yagi M., Yasuda N., 2004, ApJ, 611, 660
- Rejkuba M., 2001, A&A, 369, 812
- Schlafly E. F., Finkbeiner D. P., 2011, ApJ, 737, 103
- Schlegel D. J., Finkbeiner D. P., Davis M., 1998, ApJ, 500, 525
- Spinrad H., Sargent W. L. W., Oke J. B., Neugebauer G., Landau R., King I. R., Gunn J. E., Garmire G., Dieter N. H., 1971, ApJ, 163, L25
- Stetson P. B., 1987, PASP, 99, 191
- Stetson P. B., 1993, in C. J. Butler & I. Elliott ed., IAU Colloq. 136: Stellar Photometry - Current Techniques and Future Developments Further Progress in CCD Photometry. p. 291
- Stetson P. B., 1994, PASP, 106, 250
- van den Bergh S., 2008, AJ, 135, 1731

## APPENDIX A: GLOBULAR CLUSTER CANDIDATES PHOTOMETRY

This paper has been typeset from a  $\text{\TeX}$ /  $\text{\LaTeX}$  file prepared by the author.

**Table A1.** Photometry of “Class A” (see main text for its definition) globular cluster candidates.

ID	RA	DEC	$z'$
A1	39.53662	59.87483	15.166
A2	39.5538	59.86687	14.076
A3	39.4855	59.866	13.857
A4	39.65265	59.8602	15.442
A5	39.54418	59.83834	15.372
A6	39.54475	59.83366	14.408
A7	39.6551	59.82811	15.444
A8	39.65404	59.82696	15.874
A9	39.61442	59.82323	14.292
A10	39.70516	59.81387	14.086
A11	39.68117	59.80488	15.310
A12	39.59766	59.78675	13.126
A13	39.6995	59.77472	14.864
A14	39.55484	59.77288	15.072
A15	39.70985	59.76846	15.463
A16	39.50526	59.7392	15.010
A17	39.69786	59.73069	14.966
A18	39.66334	59.71989	13.507
A19	39.54081	59.70476	15.683
A20	39.53812	59.68151	16.392
A21	39.71023	59.67579	14.435
A22	39.50506	59.66376	14.831
A23	39.36006	59.87719	13.704
A24	39.3432	59.87714	16.218
A25	39.35974	59.87127	15.466
A26	39.4717	59.86959	15.106
A27	39.45114	59.86384	15.562
A28	39.37591	59.8423	14.705
A29	39.44419	59.83433	14.819
A30	39.4512	59.78731	14.688
A31	39.33312	59.77301	13.723
A32	39.34408	59.75875	14.683
A33	39.31949	59.74305	14.929
A34	39.40843	59.71851	15.120
A35	39.3711	59.68431	14.976
A36	39.26102	59.66222	14.941
A37	39.129	59.86855	16.035
A38	39.15034	59.86288	15.630
A39	39.05152	59.85099	15.525
A40	39.14831	59.84906	14.093
A41	39.16881	59.80869	15.874
A42	39.16513	59.80659	14.286
A43	39.06315	59.80051	16.102
A44	39.08273	59.78456	14.729
A45	39.12345	59.78061	15.616
A46	39.11763	59.76076	14.368
A47	38.92084	59.89318	15.716
A48	38.95731	59.88389	15.758
A49	38.89857	59.85564	16.311
A50	38.98749	59.84892	15.310
A51	38.81699	59.8382	14.735
A52	38.90307	59.83059	15.719
A53	38.92234	59.82842	14.717
A54	38.92963	59.81045	16.624
A55	38.88092	59.77829	16.324
A56	38.90368	59.77481	12.949
A57	38.98062	59.75234	16.631
A58	38.93923	59.74271	15.963
A59	38.87312	59.67813	16.203
A60	38.98992	59.67149	14.977
A61	38.89508	59.79097	13.505
A62	38.80202	59.87425	12.066
A63	38.59485	59.87265	15.308
A64	38.80165	59.87009	13.758
A65	38.79572	59.86403	14.714
A66	38.62018	59.85273	13.647
A67	38.74813	59.82928	15.451
A68	38.57462	59.80854	11.674
A69	38.60468	59.8037	15.287
A70	38.68509	59.78852	15.884

**Table A2.** Photometry of “Class B” globular cluster candidates.

ID	RA	Dec	$r'$	$i'$	$z'$	$\epsilon$	Notes

**Table A3.** Photometry of “Class C” globular cluster candidates.

ID	RA	Dec	$r'$	$i'$	$z'$	$\epsilon$	Notes